

Parametric longitudinal coupling between a high-impedance superconducting resonator and a semiconductor quantum dot singlet-triplet spin qubit

Received: 19 July 2021

Accepted: 20 July 2022

Published online: 15 August 2022

 Check for updates

C. G. L. Böttcher¹✉, S. P. Harvey^{1,8}, S. Fallahi², G. C. Gardner²,
M. J. Manfra^{2,3,4,5}, U. Vool^{1,6}, S. D. Bartlett⁷ & A. Yacoby¹

Coupling qubits to a superconducting resonator provides a mechanism to enable long-distance entangling operations in a quantum computer based on spins in semiconducting materials. Here, we demonstrate a controllable spin-photon coupling based on a longitudinal interaction between a spin qubit and a resonator. We show that coupling a singlet-triplet qubit to a high-impedance superconducting resonator can produce the desired longitudinal coupling when the qubit is driven near the resonator's frequency. We measure the energy splitting of the qubit as a function of the drive amplitude and frequency of a microwave signal applied near the resonator antinode, revealing pronounced effects close to the resonator frequency due to longitudinal coupling. By tuning the amplitude of the drive, we reach a regime with longitudinal coupling exceeding 1 MHz. This mechanism for qubit-resonator coupling represents a stepping stone towards producing high-fidelity two-qubit gates mediated by a superconducting resonator.

Electron spins in semiconducting materials, such as gallium arsenide (GaAs) and silicon, are promising candidates for realizing a quantum computer^{1–5}. Their long coherence times and fast control allow for high-fidelity single-qubit gates, reaching ~99.95% in single-electron spin qubits⁶. In addition to single-spin qubits, several varieties of spin qubits that are comprised of multiple spins and multiple quantum dots, including hybrid qubits, exchange-only qubits, and singlet-triplet qubits ($S-T_0$)^{7–9}, have been demonstrated. These qubits typically have increased coupling to charge, allowing fast, voltage-controlled qubit gates. The $S-T_0$ qubit is desirable due to its reduced coupling to homogeneous magnetic fields and has achieved single qubit gate fidelities of 99.5%¹⁰. While two-qubit gates have previously been demonstrated for these qubits with a fidelity of ~90%¹¹, these gates are

slow and rely on nearest neighbor coupling, limiting scalability. Much attention is now focused on achieving long-range two-qubit coupling, for example, using arrays of quantum dots for charge transfer^{12–15} or a superconducting resonator by adapting circuit QED (cQED) techniques, thus making electron spins a scalable platform for quantum computing technology.

Extensive work on implementation of cQED techniques in spin qubits has recently been demonstrated^{16–22}, and despite promising progress^{23,24}, a two-qubit gate has not yet been achieved. The qubit-resonator coupling explored relies on the strong electric fields produced by a resonator, which couple to the dipole moment of a spin qubit. The most commonly considered coupling scheme is a transverse coupling between the spin and resonator, where an excitation of

¹Department of Physics, Harvard University, Cambridge, MA 02138, USA. ²Department of Physics and Astronomy, Purdue University, West Lafayette, IN 47907, USA. ³School of Materials Engineering, Purdue University, West Lafayette, IN 47907, USA. ⁴Birck Nanotechnology Center, Purdue University, West Lafayette, IN, USA. ⁵School of Electrical and Computer Engineering, Purdue University, West Lafayette, IN 47907, USA. ⁶John Harvard Distinguished Science Fellowship, Harvard University, Cambridge, MA 02138, USA. ⁷Centre for Engineered Quantum Systems, School of Physics, The University of Sydney, Sydney, NSW 2006, Australia. ⁸Present address: Stanford University, Stanford, CA 94305, USA. ✉e-mail: cboettcher@g.harvard.edu

the spin qubit can be exchanged for a resonator excitation²⁵. This requires the qubit energy splitting to be near the resonator frequency, and typically leads to lower lifetimes due to the Purcell effect. In recent years, there has therefore been growing interest in alternative coupling schemes based on longitudinal interactions, which do not have these limitations^{26–32}. Spin qubits are highly amenable to longitudinal coupling, although it has not been demonstrated experimentally before. In previous theoretical work³³, such a coupling scheme was explored for singlet-triplet qubits, predicting encouraging average two-qubit gate fidelities of 96% and gate times of the order of 10 ns. This approach, analogous to the Mølmer–Sørensen gate³⁴ that is commonly used for high fidelity two-qubit gates in ion trap qubits^{35,36}, relies on a purely longitudinal interaction between the spin and resonator to produce a two-qubit coupling.

In this article, we demonstrate experimental efforts towards achieving longitudinal coupling between a singlet-triplet ($S-T_0$) qubit and high-impedance superconducting resonator. We show that our device has significant longitudinal coupling, tunable by a direct drive, in addition to a fixed spurious dispersive coupling. We present a measurement sequence that allows one to separate each coupling term and measure their individual coupling strengths. The sequence takes advantage of the qubit's exquisite sensitivity, enabling us to extract resonator parameters as well as qubit-resonator coupling strengths. By tuning the drive amplitude we can achieve a longitudinal coupling strength that exceeds the dispersive term, which is an exciting regime within hybrid circuit QED systems as well as an important stepping stone towards producing two-qubit coupling mediated by a resonator.

Results

Design of the device

The device consists of two double quantum dots (DQDs) formed in Si-doped GaAs/AlGaAs heterostructure with a two-dimensional electron gas (2DEG) located ~ 90 nm below the surface. The two DQDs are coupled to a high-impedance superconducting resonator and separated by $100\mu\text{m}$ as illustrated in Fig. 1a. The 2DEG is removed using chemical etching in a large area, leaving only a separate island (mesa) for each DQD. The two spatially separated DQDs are each tuned to be $S-T_0$ qubits, and due to their large distance from one another, the only coupling between them is mediated by a superconducting resonator. The resonator climbs the mesa and capacitively couples to

the left and right DQD (Fig. 1b), marked QL and QR in Fig. 1a. The resonator is fabricated in the etched area from a 20 nm superconducting film made of niobium nitride (NbN) and meandered across the sample. Using a thin film of NbN as the resonator material, one can obtain a large kinetic inductance, L_K . The kinetic inductance, $L_K = (m_e/2n_s e^2)(l/A)$ ³⁷, depends on the superfluid density, n_s , and scales with resonator length l and cross-sectional area A , thus we achieve a high impedance close to $Z_r = \sqrt{(L_K + L_m)/C_r} \sim 2$ k Ω for a resonator design with a meander width of 150 nm (Fig. 1c). The retracted ground plane minimizes resonator capacitance C_r , and magnetic inductance L_m , such that the resonator is largely dominated by its kinetic inductance. The resonator's high impedance makes it well suited for coupling to systems such as electrons in DQDs, which have small electric dipole moments.

Our $S-T_0$ qubits each consist of two electrons trapped in a DQD defined using electrostatic gates for static potential confinement shown in Fig. 1d. The logical subspace of the qubits consists of the singlet, $|S\rangle = (|\uparrow\downarrow\rangle - |\downarrow\uparrow\rangle)/\sqrt{2}$ and triplet $|T_0\rangle = (|\uparrow\uparrow\rangle + |\downarrow\downarrow\rangle)/\sqrt{2}$, states. We apply a static in-plane magnetic field of ~ 700 mT making higher energy states energetically inaccessible. The energy splitting $J(\epsilon)$, splits S from T_0 and is tuned on a nanosecond timescale by the difference in chemical potential ϵ , set by the two radio frequency (RF) gates, labeled RF1 and RF2, that enable fast pulsing and control.

Readout in our device is different from what is typically done in circuit QED experiments. We do not include a direct feedline port to control and read out the resonator, simplifying the design. Rather, the qubits are measured using a sensor dot proximal to each DQD to measure the charge state of the DQD. The resonator is excited using the DQD gates that are capacitively coupled to it and described in the next section.

Probing the coupled resonator-qubit system

We introduce a measurement technique, based on a Hahn-echo-like sequence, to characterize the qubit-resonator interaction. Due to its increased coherence time, the Hahn-echo pulse sequence offers greater sensitivity than a typical Ramsey experiment and can be used, for instance, to characterize the noise environment seen by the qubit^{38–40}. It can also be used to measure changes in the exchange splitting of the qubit, $J(\epsilon)$, between the first and second half of the pulse sequence, which we use to extract changes in the electrostatic environment of the qubit.

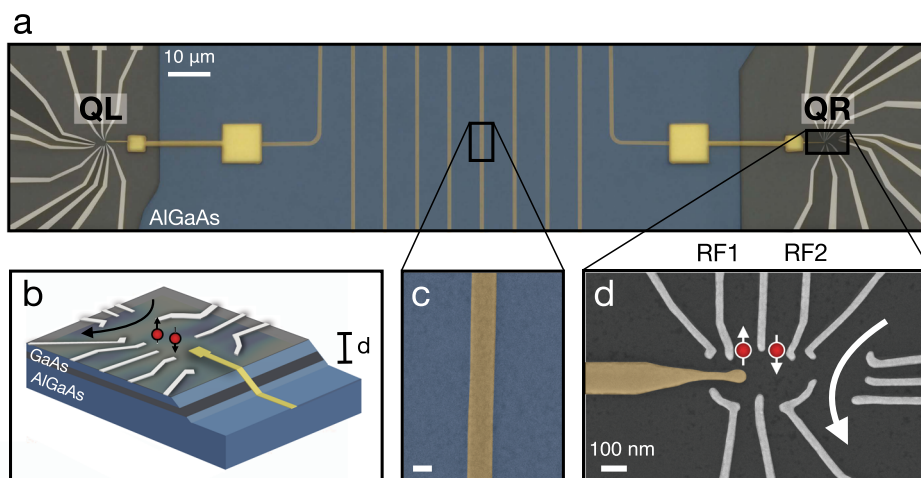


Fig. 1 | Device layout. **a** False colored scanning electron microscope (SEM) image of two double quantum dots (DQDs) that are placed at each end of a superconducting resonator made from thin film NbN and constitute left and right qubit (QL and QR). The resonator is meandered across the etched part of the sample where 2DEG has been removed. **b** Illustration of the resonator climbing the edge of the etched region with a height of $d \sim 90$ nm. It couples capacitively to the DQD

through the electric field of the resonator. **c** To maximize the coupling, the resonator impedance can be enhanced by NbN, a material with large kinetic inductance, and reducing the center conductor width to 150 nm. **d** SEM image showing right DQD. Each DQD requires a set of DC gates to define the quantum dots and a set of RF gates (RF1 and RF2) to have fast control of the $S-T_0$ energy splitting.

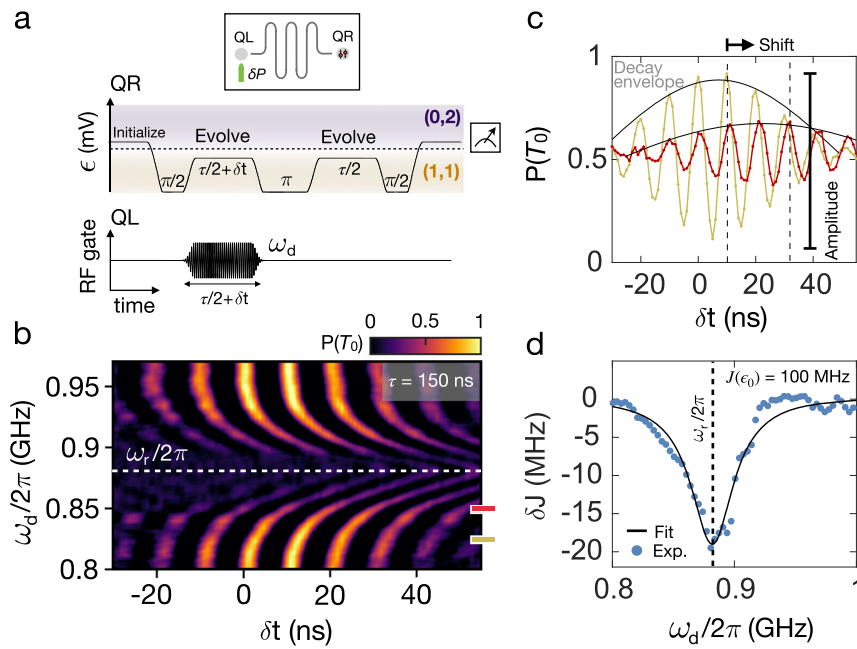


Fig. 2 | Measurement sequence for probing resonator-qubit coupling. **a** Echo pulse sequence used to measure the exchange splitting of right qubit (QR) while driving the resonator using the RF gate of left qubit (QL). Gate is marked dark green in cartoon inset. Purple/orange shading is to indicate DQD occupation (0,2)/(1,1). **b** Exchange oscillations, shown by plotting the triplet probability $P(T_0)$ as a function of δt , is measured at several drive frequencies and indicate the qubit-resonator

interaction near the resonator frequency ω_r . **c** Two line cuts at different values of drive frequency (ω_d) reveal a phase shift and rapid qubit dephasing when the drive frequency is close to the resonator frequency $\omega_r/2\pi = 0.88$ GHz. The decay envelopes fit to a Gaussian decay function given by T_2^* . **d** Extracted values of the change in energy splitting, δJ , as a function of ω_d fit to a Lorentzian function to extract resonator decay rate κ , resonance frequency ω_r , and coupling strength χ .

The electrostatic environment of each qubit is determined by the control lines together with the resonator. We can control each qubit by applying voltages to the nearby RF gates, with which we apply a static potential ϵ_0 and a direct RF drive $\epsilon_d \cos \omega_d t$, where ω_d is the drive frequency. We will use superscripts L,R on the drive amplitude ($\epsilon_d^{L,R}$) to indicate if the drive is sent to the left or right qubit. In addition, the qubit is sensitive to the voltage fluctuations of the resonator $V_r = V_0(a + a^\dagger)$ where a is the resonator annihilation operator and $V_0 = \sqrt{\hbar Z_r / 2\omega_r}$ is the zero-point voltage fluctuation, set by the frequency of the resonator ω_r and its impedance Z_r . The chemical potential at each quantum dot can thus be expressed as $\epsilon = \epsilon_0 + \epsilon_d \cos \omega_d t + \epsilon_c V_r$, where ϵ_c is the lever-arm of the resonator fluctuations on the qubit. Moving to an interaction picture relative to the drive frequency ω_d , the resulting qubit energy splitting $J(\epsilon)$ leads to the qubit-resonator Hamiltonian (see ref. 33) given by

$$H_{\text{int}} = \hbar \Delta a^\dagger a + J(\epsilon_0) \sigma_z + \frac{1}{2} g (a + a^\dagger) \sigma_z + \frac{1}{2} \chi a^\dagger a \sigma_z, \quad (1)$$

where $\Delta = \omega_r - \omega_d$ is the detuning, and $g = \frac{d^2 J}{d\epsilon^2} \Big|_{\epsilon_0} c_r V_0 \epsilon_d$ and $\chi = \frac{d^2 J}{d\epsilon^2} \Big|_{\epsilon_0} c_r^2 V_0^2$ are the two coupling strengths. The Hamiltonian can be written in the simplified form $H = \hbar \Delta a^\dagger a + \tilde{J} \sigma_z$ by defining the modified qubit energy splitting $\tilde{J} = J(\epsilon_0) + \frac{1}{2} g (a + a^\dagger) + \frac{1}{2} \chi a^\dagger a$, where the last two terms represent the qubit interaction with the resonator. We refer to the first term, proportional to g , as the longitudinal term, and note that it can be tuned by the amplitude of the drive, ϵ_d . The second term, proportional to χ , which we call the dispersive term, is independent of the drive. Following ref. 33, we are ultimately interested in implementing a two-qubit coupling in the case where $c_r V_0 / \epsilon_d \ll 1$, i.e., where the dominant interaction is longitudinal and set by coupling strength g . However, to fully characterize our device, we wish to determine each qubit's individual coupling strengths g and χ to the resonator. We therefore focus primarily on the interaction of a single qubit with the

resonator. Our device architecture allows us to independently measure each qubit and control the two coupling terms, simply by driving the resonator using near and far qubit RF gates with respect to the active qubit, as we now describe.

We first consider a measurement that allows us to characterize the dispersive term χ . To measure \tilde{J} , the standard Hahn-echo sequence is modified by introducing a drive of the resonator during the first evolution time $\tau/2$ of QR as illustrated in Fig. 2a. As indicated in the device sketch, we use an RF signal with power δP to turn on the gate marked in green on the left side of the resonator, the opposite antinode of QR. The left qubit, QL, is kept far detuned, and it can effectively be ignored for the remainder of the paper. Because there is no direct drive of QR in this experiment, only coupling through the resonator, we expect $g = 0$ and that this sequence will generate a coupling given by only the dispersive term with strength χ . As the frequency ω_d of the RF pulse is tuned near the fundamental frequency of the resonator ω_r , the resonator will be excited and interact with the qubit. The qubit's energy splitting is modified by the qubit-resonator interaction to be J_1 , which differs from the splitting in the second half of the sequence where RF excitation is turned off, J_2 . The echo measurements reveal a decay envelope, captured by sweeping the length of the first pulse by small increments of δt . The maximum amplitude reveals the extent to which the state has dephased, while the shape of the envelope and width arise from an effective single-qubit rotation for a time δt and envelope associated with T_2^* ⁴⁰. In Fig. 2b we plot the exchange oscillations measured for a set of drive frequencies and observe a significant phase shift of the decay envelope when $\omega_d - \omega_r$. The shape is well-captured by a Gaussian decay function similar to ref. 40 with $T_2^* \sim 250$ ns, presented in Fig. 2c for two line cuts, one taken far off resonance at 0.82 GHz and one taken close to resonance at 0.85 GHz. There are two clear effects. First, a significant shift of the envelope close to resonance suggests an accumulated phase during the RF on-sequence due to the qubit's interaction with the resonator. The magnitude of the phase shift is

given by $\theta = (J_1 - J_2)\tau/2 = \delta J \tau/2$. We fit the oscillations and plot δJ as a function of drive frequency in Fig. 2d, which is well described by a Lorentzian function. We extract the resonator parameters $\omega_r/2\pi = 0.88\text{GHz}$ and $\kappa/2\pi \approx 50\text{MHz}$ corresponding to a $Q = \omega/\kappa \approx 20$ discussed later, as well as the dispersive coupling strength $\chi/2\pi \approx 0.2\text{MHz}$ for a qubit detuning leading to $J(\epsilon_0) \approx 100\text{MHz}$ and fixed drive amplitude. The data show an additional effect: a significant suppression of the oscillation amplitude closer to resonance ω_r (Fig. 2c), suggesting a rapid dephasing of the qubit. We return to this effect in Sec. V.

Longitudinal coupling

Having characterized the drive-independent dispersive coupling term, we now turn our focus to the longitudinal term that would form the basis for a two-qubit coupling scheme. To generate a longitudinal coupling with coupling strength g , a second drive is introduced to simultaneously modulate the qubit, QR, at frequency ω_d with a tunable drive power δP , while keeping the left drive power fixed (illustrated by the device sketch in Fig. 3). Drive frequency of left and right drive are swept simultaneously, thus ω_d represents both drive frequencies. By systematically increasing the right drive power, δP , we can study the competition between the longitudinal and dispersive coupling terms, g and χ .

In Fig. 3a, b exchange oscillations for two values of δP are observed, similar to Fig. 2a. The oscillations reveal an asymmetry in the shift of the echo envelope around the resonance frequency that is enhanced with larger drive power. Again, we observe that qubit dephasing on resonance increases with power; we return to this effect in the next section.

By solving the master equation of the coupled system described by the Hamiltonian in Eq. (1), an asymmetry similar to the one seen in the data is found; see Fig. 3c, d. The system is solved by including damping from the resonator, $\kappa/2\pi = 50\text{MHz}$, and tuning the ratio between the two coupling terms. This reveals that when g is large, the asymmetry is pronounced, suggesting this effect is entirely due to the longitudinal term in Eq. (1).

This measurement allows us to investigate the competition between the longitudinal and dispersive terms. We can understand the qubit-resonator interaction by using a simple semi-classical description of the state of the resonator as a coherent state with complex amplitude $\alpha = |\alpha|e^{i\theta} = \frac{\epsilon_d}{\Delta + i\kappa/2}$. With the resonator state described this way, the qubit energy splitting \tilde{J} can be expressed as

$$\tilde{J} = J(\epsilon_0) + g \text{Re}(\alpha) + \chi |\alpha|^2. \quad (2)$$

The second term on the right side is proportional to the real part of α and will therefore change sign with detuning, while the last term, which is proportional to the square of the amplitude, will remain positive for all values of detuning. This behavior explains the asymmetry of the data shown in Fig. 3a, b.

Using this simple model, we fit the extracted phase shifts, δJ , from Fig. 3a, b to Eq. (2) for several values of the drive power, as shown in Fig. 4a. We observe good agreement between the model and data, and accurately capture the asymmetry around resonance. The coupling strengths are fit parameters in the model and presented in Fig. 4b as a function of the right qubit drive power ϵ_d^r . We can express the coupling parameters in terms of the average number of photons $\langle n \rangle$ generated by the drive power from the relation $\epsilon_d = \sqrt{\langle n \rangle} \kappa/2$. From the definitions of the two coupling coefficients, g and χ , we expect χ to be independent of drive power while g should increase linearly with drive power. Data from our experiment are consistent with this prediction that χ is constant, independent of power, with an average value of $\chi/2\pi \approx 0.4\text{MHz}$. For g , we observe $g/2\pi \approx 0.15\text{MHz}$ at lowest value of drive power and $g/2\pi \approx 1\text{MHz}$ at the highest value. The expected increase is linear with ϵ_d^r . We note the larger error bars in the high drive power regime.

To further explore the competition between g and χ , the left drive is now varied while the right drive is fixed. The result is presented in Fig. 4c, and we note that there is no asymmetry apparent around resonance even at the highest power. In this regime, $g/\chi \approx 0.3$, so that χ is the dominant signal. The fitting procedure to Eq. (2) is repeated for this coupling regime and coupling strengths are extracted and presented in Fig. 4d as a function of ϵ_d^l . Our model predicts that both coupling strengths are constant, independent of left drive power ϵ_d^l , and the data are consistent with prediction with only small variations in this range of power. The average value for $\chi/2\pi \approx 0.4\text{MHz}$ is consistent with the results shown in Fig. 4b and $g/2\pi \approx 0.15\text{MHz}$ is similar to the lowest value of g observed previously.

Driving the resonator using near and far RF gates with respect to the active qubit allows us to separate the contributions from the two coupling terms. We can then consider tuning to the regime such that the dominant effect is longitudinal, with $g/2\pi \approx 1\text{MHz}$, which is done by turning on the maximum drive power. Due to direct coupling between the RF gate and qubit, we are limited in further increasing the drive power as it will interfere with state preparation and operation of our qubit. Other ways to enhance coupling strength are to increase the impedance of the resonator, thus enhancing the voltage fluctuations at the antinode, and to increase the lever arm, c_r . Lastly, we note that both coupling strengths also depend on $J(\epsilon)$. Using the empirical approximation $J(\epsilon_0) \propto J_0 \exp(\epsilon/\epsilon_0)$, and hence $\chi, g \propto \frac{d^2 J}{d\epsilon^2} \Big|_{\epsilon_0} - J/\epsilon_0^2$. As a result the couplings will scale linearly with the J , so it seems advantageous to increase J as much as possible. The expected scaling with J can be observed by comparing the single drive result in Fig. 2d with the results shown in Fig. 4. Figure 2 was produced with a qubit detuning of $J(\epsilon_0) \approx 100\text{MHz}$ leading to $\chi/2\pi \approx 0.20\text{MHz}$, while Fig. 4 was produced with $J(\epsilon_0) \approx 200\text{MHz}$, leading to $\chi/2\pi \approx 0.40\text{MHz}$, consistent with linear scaling. This approach may not improve gate fidelities because qubit noise increases with a similar scaling⁴⁰. Instead, this is an optimization problem discussed in ref. 33, where an optimal drive is found by considering the type of qubit noise measured for $S-T_0$ qubits in GaAs⁴⁰, leading to the maximum two-qubit gate fidelity for this system.

Measurement-induced dephasing. Finally, we turn to the rapid dephasing of the qubit when the drive frequency is tuned close to that of the resonator, $\omega_d \approx \omega_r$. This provides us with an additional tool with which to study the interaction between qubit and resonator. We assume qubit noise is as described in ref. 40 and the remaining noise can be attributed to the interaction between qubit and resonator. Figure 3 shows that the dephasing rate is enhanced with drive and the width is of the order κ . Such effects have previously been explored by looking at the resonator back-action on the qubit, an effect known as measurement-induced dephasing^{41,42}.

Formally, this requires studying photon noise, or fluctuations in the photon number operator $n = a^\dagger a$, which couples to σ_z with coupling strength χ , reflecting noise through the dispersive coupling to the resonator⁴². However, since there are both dispersive and longitudinal coupling terms, fluctuations in the operator $x = a + a^\dagger$ that couples to σ_x with a coupling strength g must also be considered. In both cases, the limit $g, \chi \ll \kappa$, so the dephasing can be derived using Fermi's Golden Rule, and is written as follows⁴³:

$$\Gamma_\phi = \Gamma_\phi^x + \Gamma_\phi^g + \Gamma_\phi^{gx} \quad (3)$$

$$= \frac{\chi^2}{2} S_{nn}^x(\omega=0) + \frac{g^2}{2} S_{xx}^g(\omega=0) + g\chi S_{xn, nx}^{gx}(\omega=0)$$

The first two terms arise from pure χ and g effects, respectively, and the third as a result of their cross coupling. Γ_ϕ can be derived as a function of detuning by calculating the power spectral densities (described in "Methods"), $S_{AB}(\omega) = \int_{-\infty}^{\infty} dt C_{AB}(t) e^{-i\omega t}$ and the Fourier transform of the correlation functions, $C_{AB}(t) = \langle A(t)B(0) \rangle - \langle A \rangle \langle B \rangle$

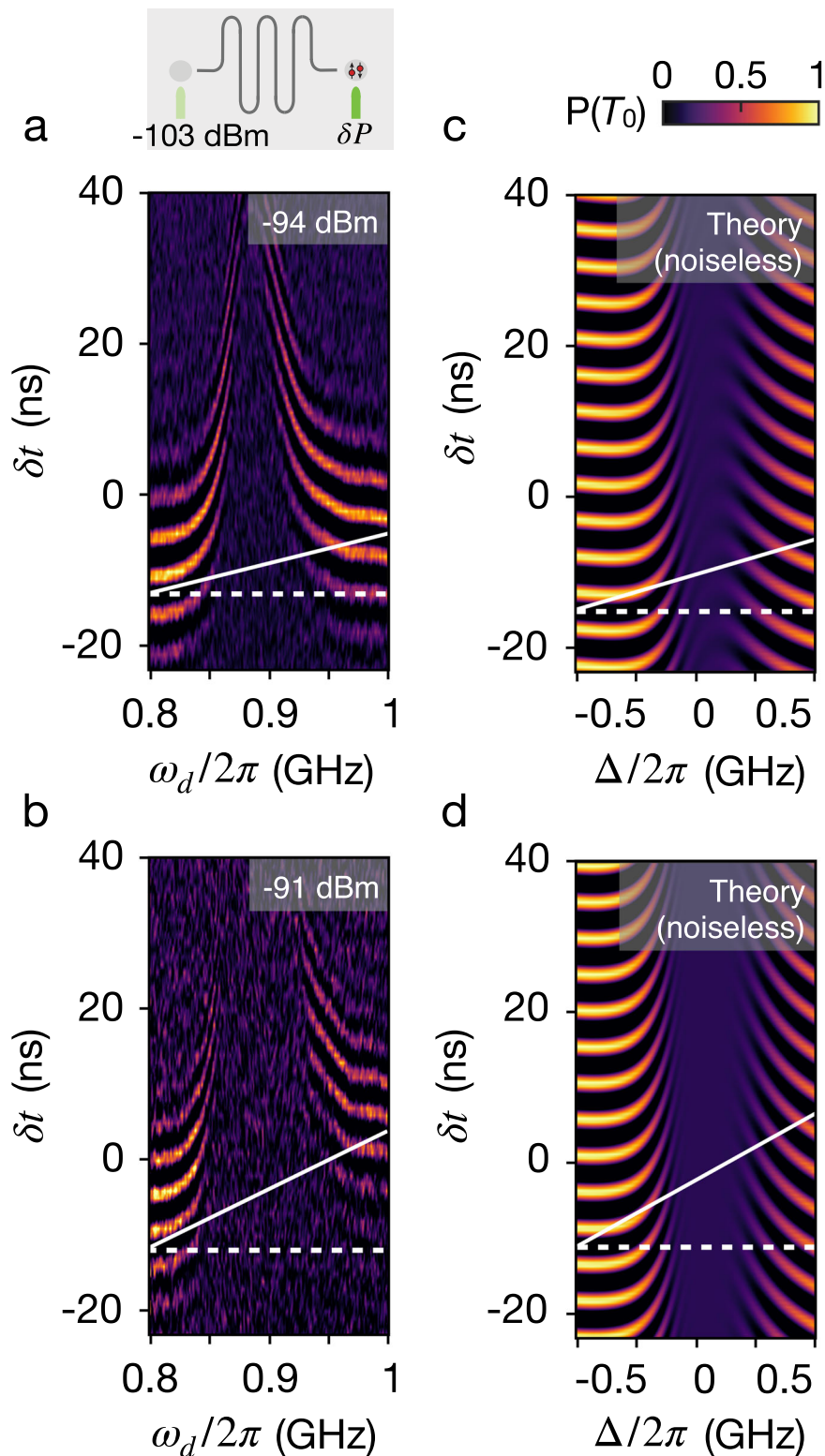


Fig. 3 | Exchange oscillations in double-driven regime. Inset: We drive the resonator by sending a RF signal to the gate placed at its right antinode (dark green) with power δP and simultaneously sending a signal to the gate at the left antinode (light green), the opposite side of the active qubit, which is kept at a fixed power. **a** Exchange oscillations when $\delta P = -94$ dBm reveal a large phase shift near ω_r , marked with the white dashed line. The asymmetry around resonance is marked by a white line tilted with respect to a horizontal reference line (white dashed line).

b Power sent to the right gate is increased to $\delta P = -91$ dBm leading to a larger phase shift and an enhanced asymmetry. **c** Solutions to the master equation for the coupled qubit-resonator system produce a similar asymmetry to (a) when the g term is the dominant coupling term in Eq. (1). **d** By further increasing the strength of g , the simulations reproduce the enhanced asymmetry in (b), corresponding to the highest drive power. Simulations do not include an explicit dephasing term for the qubit.

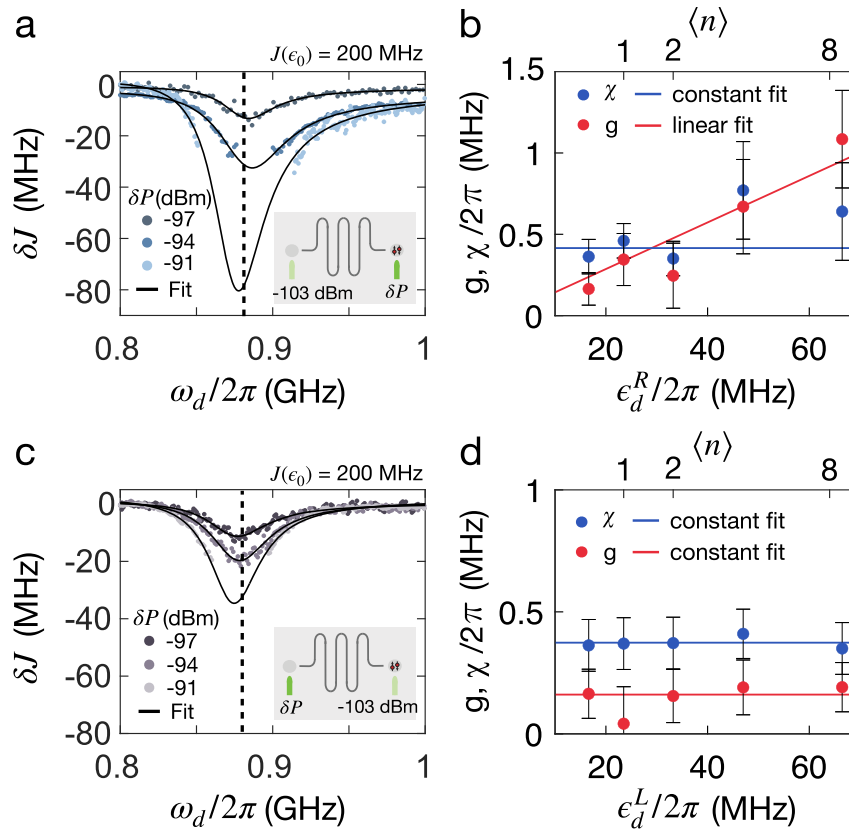


Fig. 4 | Parametric longitudinal coupling. **a** Extracted δJ as a function of ω_d when right drive power is varied (dark green) while left drive power is kept constant (light green), as indicated in figure inset. The asymmetry around the resonator frequency ω_r (black dashed line) is greatly enhanced with drive power. To extract coupling strengths g and χ , presented in **(b)**, we fit to our model, Eq. (2), as a function of drive power ϵ_d (bottom horizontal axis) or of average photon number $\langle n \rangle = (2\epsilon_d/\kappa)^2$ (top horizontal axis). This model predicts the coupling strength g to be tunable with linear dependence on the right drive amplitude (a square-root dependence on average photon number), while predicting a constant value of χ .

Solid lines show linear and constant fits for g and χ respectively. At high power, g exceeds χ , thus providing the dominant coupling to the resonator. We note the larger error bars in the high drive power regime, which is due to increased dephasing at high drive powers, thus limiting fitting to exchange oscillations and extraction of δJ . **c** Figure inset: left drive power is varied, keeping right drive fixed. Extracted δJ as a function of ω_d shows a very symmetric resonance and fits to the model lead to the extracted coupling strengths presented in **(d)**. Coupling strengths g and χ both fit well to constant values independent of the left drive power, as predicted by our model.

$\langle B(0) \rangle$, yielding:

$$\Gamma_\phi = \frac{g^2 \frac{\kappa}{2}}{\Delta^2 + (\frac{\kappa}{2})^2} + \frac{\epsilon_d^2 \chi^2 \frac{\kappa}{2}}{(\Delta^2 + (\frac{\kappa}{2})^2)^2} + \frac{2g\chi\epsilon_d \frac{\kappa}{2} \Delta}{(\Delta^2 + (\frac{\kappa}{2})^2)^2}. \quad (4)$$

Similar to the g term in Eq. (2), the third term changes sign with detuning, leading to an asymmetry in the dephasing rate around resonance, but in contrast to Eq. (2), this effect requires both a dispersive and longitudinal interaction with the resonator. This asymmetry is observed in the data. Figure 5a, b shows the maximum amplitude extracted for each drive frequency and for two different drive powers. Using Eq. (4), we model the amplitude decay, $A = A_0 e^{-\Gamma_\phi(\tau/2 + \delta t)}$, using qubit-resonator coupling strengths and resonator parameters extracted from the phase-shift model that we presented in Eq. (2), which is an independent theory. We extract the maximum amplitude of the exchange oscillations presented in Fig. 3 and plot them with the result obtained from the model in Eq. (4); we find that they show excellent agreement. The asymmetry is present when we have both longitudinal and dispersive effects (Fig. 5a). The asymmetry is proportional to the last term in Eq. (4), in contrast to the first two terms, which only scale with g and χ , respectively, demonstrating the significant contribution of the longitudinal coupling term to the dynamics of the spin-resonator system.

Discussion

We have demonstrated that it is possible to produce a longitudinal coupling to the resonator that exceeds the dispersive term in strength. However, the resonator decay time is the limiting factor in the current device, and we were not able to generate a two-qubit coupling. We now describe the reasons for this limitation, and consider several paths forward for generating two-qubit coupling by improving system characteristics

The two-qubit gate proposed in ref. 33 requires $g \gg \chi$. Since g is proportional to the drive amplitude, the coupling strength can be tuned to reach a regime where the longitudinal coupling dominates, as discussed previously (see Fig. 4b), by increasing the drive such that $\epsilon_d \gg c_r V_0$. In this regime, where the dispersive term proportional to χ is negligible, two-qubit coupling can be generated by placing two qubits at opposite antinodes of the resonator, each longitudinally coupled to it. This leads to the following two-qubit Hamiltonian³³

$$H_{12}/\hbar = \Delta a^\dagger a + g_1(a + a^\dagger)\sigma_{z1} + g_2(a + a^\dagger)\sigma_{z2}. \quad (5)$$

For a full derivation of the two-qubit gate we refer the reader to our previous work in ref. 33. A two-qubit gate is generated by driving the system slightly detuned from the resonator frequency. This allows one to make a closed loop in phase space that corresponds to an accumulated relative phase $\Phi_{12} = \frac{g_1 g_2}{2\hbar^2 \Delta} t_g$. When $\Phi_{12} = \pi/4$, a CPHASE gate is implemented on the two-qubit system. Disentangling the

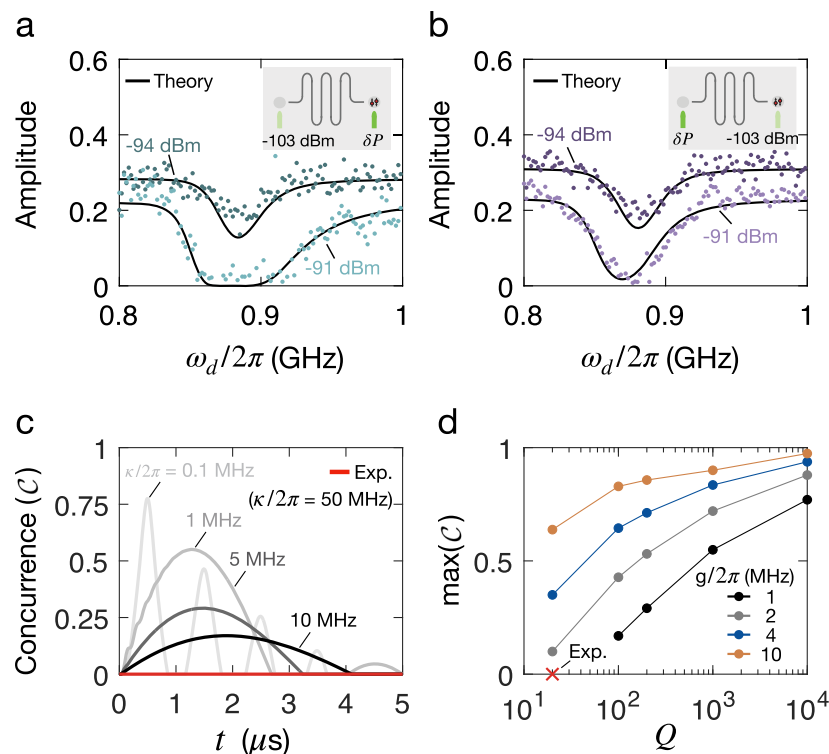


Fig. 5 | Qubit-resonator entanglement and paths towards two-qubit coupling.

Qubit dephasing is analyzed by considering its coupling to photon noise through entanglement with the resonator, also known as measurement-induced dephasing. **a, b** Maximum amplitude of exchange oscillations as a function of ω_d for two driving cases, illustrated in the figure insets. When the right drive is varied (**a**), an asymmetry is observed in the qubit dephasing, which is captured by the model presented in Eq. (3). Parameters extracted from the phase shift model in Eq. (2) are

used in the model instead of fitting the data. When the left drive is varied (**b**), the qubit dephasing is symmetric and well captured by the model. **c** The concurrence is extracted for a set of resonator decay rates. Improving the resonator lifetime greatly enhances two-qubit coupling. **d** Maximum concurrence as a function of resonator Q for a set of coupling strengths shows a finite two-qubit entanglement is achieved at $Q=20$ by increasing $g/2\pi$ to 2 MHz, a doubling of the experimentally-achieved coupling strength.

resonator from the system requires that a full loop is completed, hence setting $\Delta \cdot t_g = 2\pi m$, where m is the number of loops in the resonator phase space and t_g is the gate time. This leads to the optimal detuning $\Delta = 2\sqrt{m g_1 g_2}$. Using experimental parameters for the coupling strength g , we calculate the entanglement that can be generated by this two-qubit gate (as measured by the concurrence) for several different resonator decay rates by solving the master equation for the two-qubit interaction described by Eq. (5) and including cavity decay. The results are presented in Fig. 5c, where for each point the optimum detuning is chosen such that it maximizes the concurrence. In the current device, $\kappa/2\pi \approx 50$ MHz giving $Q = \omega_d/\kappa \approx 20$, so it is clear from examination of Fig. 5c that resonator decay is the main limitation. Since resonator decay dominates gate infidelity, increasing the number of loops n improves the two-qubit entanglement as it requires a larger Δ and thus lower photon number during the gate. However, this also increases the gate time, leading to an optimal m set by balancing the resonator decay and limited qubit coherence. For this simulation, we assumed typical spin qubit coherence values $T_1 = 100 \mu\text{s}$, $T_2 = 10 \mu\text{s}$ ⁴⁰, and used the corresponding optimal m values.

While our analysis shows that two-qubit entanglement can be achieved even for modest values of resonator quality factor, the low value of $Q \approx 20$ is currently the main limiting factor in the present device. Several components in the circuit could be contributing to reducing Q in this experiment. A resonator-bias line was added to give the resonator a DC voltage bias, enabling better tuning of the quantum dot potentials, which allowed both DQDs on the same resonator to be tuned into $S-T_0$ qubits simultaneously^{17,44}. With the resonator being very close to each DQD, this can lead to warping of the potential landscape the DQDs are sitting at, making tuning of both qubits challenging. The bias line helps to offset the influence of

the resonator, enabling improved control of tuning. This has previously been a major challenge in the research towards performing two-qubit entanglement through a resonator in spin qubits. However, imperfections in the design of the bias line could affect resonator Q (details are described in Methods). In addition, each qubit's DC gates at the voltage antinodes capacitively couple to the resonator, potentially creating photon leakage paths. These could be further decoupled by implementing LC filters^{17,44,45}. Also, coupling to the lossy substrate could induce surface loss, and chemical processing of the surface could lead to surface roughness, both of which reduce the Q . These issues would be mitigated by moving to pristine and low-loss silicon substrates, which can be implemented either with Si-Ge based spin qubits or by using flip-chip methods. In the future, when a high Q regime is reached, the low resonance frequency obtained in this experiment may be a concern due to coupling to thermal photons. This can be mitigated by moving to higher frequencies, which is set by the resonator length.

Additionally, two-qubit entanglement could be improved by increasing the longitudinal coupling g , as illustrated in Fig. 5d. By doubling the coupling strength relative to what was achieved in this experiment, a finite entanglement can be obtained with the current resonator decay time. Further increasing to $g/2\pi = 10$ MHz would significantly enhance the two-qubit coupling, achieving concurrence above 50% at lowest Q of 20 and above 90% for values of resonator Q above 1000, already obtained in other silicon-based spin qubit systems^{16,17,22}. Increasing g can be done, for instance, by switching to other superconducting materials with higher kinetic inductance, such as granular aluminum, which has $L_K \approx 1-3 \text{ nH}/\square$ ^{46,47}, two orders of magnitude higher than NbN. This would greatly enhance the impedance of the resonator and induce larger voltage fluctuations at the

resonator's antinode proximal to the qubit without increasing the dephasing directly.

In conclusion, we have presented a spin qubit-resonator system with a tunable longitudinal coupling, and shown that we are able to enter a longitudinally dominant coupling regime. Our measurement sequence allows the qubit-resonator dynamics to be investigated in multiple ways, revealing pronounced effects due to the longitudinal coupling and allowing us to extract the individual coupling strengths of the longitudinal and dispersive terms. This is an experimental demonstration of a longitudinal coupling between a semiconductor-based spin qubit and superconducting resonator that to our knowledge has otherwise only been explored theoretically. Although a $S-T_0$ qubit was used here, it is possible to use any spin qubit provided it has gateable, charge-like states. The results are therefore important steps towards generating a two-qubit coupling through longitudinal coupling and project promising results for a two-qubit gate fidelity by improving resonator parameters such as decay rates by moving to low-loss silicon substrates or increasing the impedance by utilizing higher kinetic inductance materials.

Methods

Resonator fabrication

The 2DEG was gently removed using a chemical etching process that involves diluted phosphoric etch in H_2O and H_2O_2 . Phosphoric acid etches GaAs isotropically leaving the angle of the edge at 45° , for a smooth climb of the resonator to the DQD. Using sputtering techniques, a thin film of NbN is deposited in the etched area between the two mesas, each of which hosts a DQD. The resonator's climb of the mesa is performed in a second fabrication step, connecting the portion of the resonator residing on the etched part of the sample and the part that capacitively couples to the DQDs on the mesas, thus reducing the potential for resonator disconnects during the climb. The resonator is fabricated with a DC voltage bias line which is placed at the voltage node and should therefore not affect the Q of the resonator. However, the bias line could provide a leakage path for photons in the resonator. To prevent this, the bias line was designed with an LC filter, adapting designs also described in^{17,44}. Here, the resonator bias line is added to the resonator voltage node, then filtered using an inductor in series with a capacitor, constituting an LC filter on the bias line to prevent loss of photons.

Estimating the drive

The total attenuation in the measurement setup is estimated as follows: 33 dB attenuation has been added to the coax line inside our dilution fridge with 20 dB on the 4K plate, 10 on the 100 mK plate and 3 dB on the mixing chamber plate. We use a Hittite RF generator that is connected to an IQ circuit with a total attenuation of 25 dB. This goes to a splitter on the output of an Arbitrary Waveform Generator (AWG 5014C). The splitter has an internal loss of 6 dB and an additional 16 dB of attenuation was added to the output port before entering the fridge. The resonator and qubit are driven using one of the RF gates. Using the Sonnet software package to simulate the gate geometry with the resistivity of Ti/Au, we further include 20 dB of loss due to the RF gate itself. Altogether, we find the total attenuation of the circuit to be ~ 100 dB.

Several values of the drive power are used in the experiment to drive the qubit-resonator system into different regimes. As an example, consider the total power used in the experiment of -97 dBm converted to 1.58×10^{-13} Watts. Then using the relation between power and number of photons⁴¹:

$$\langle n \rangle = 4PQ^2 / (\hbar\omega_r^2 Q_c). \quad (6)$$

The coupling quality factor, Q_c , is estimated from a simulation of the device structure, which gives $Q_c = 31, 457$. An estimate of the total

loaded Q is found from experimental values $Q = \omega_r / \kappa = 18.72$. This gives an estimate for the average number of photons in the resonator for a given drive power to be $\langle n \rangle = 2.19$. From $\langle n \rangle$ and κ we find the drive amplitude is given by $\epsilon_d / 2\pi = \sqrt{\langle n \rangle} \kappa / 2 = 34.74$ MHz.

Calculating power spectral densities

We compute the power spectral densities used in the dephasing model described by Eq. (3) of the main text, where we consider the limit $g, \chi \ll \kappa$. The dephasing is attributed to photon noise, or fluctuations in the photon number operator $n = a^\dagger a$ and $x = (a + a^\dagger)$ that couples to σ_z with a coupling strength χ and g respectively. Additional terms arise from cross couplings, which will be computed here as well. Calculations of the power spectral densities, $S_{AB}(\omega) = \int_{-\infty}^{\infty} dt C_{AB}(t) e^{-i\omega t}$, for each dephasing term in Eq. (3) are carried out by first computing the correlation functions, according to the general definition

$$C_{AB}(t) = \langle A(t)B(0) \rangle - \langle A(t) \rangle \langle B(0) \rangle. \quad (7)$$

Then, we move into the displacement frame $d = a - \beta$ ($d^\dagger = a^\dagger - \beta^*$) where we define a coherent state β such that the cavity equilibrium state is $|0\rangle$. We calculate for $A = B = x$ and find that the dependence on β cancels, yielding

$$C_{xx}^g(t) = \langle d(t)d^\dagger(0) \rangle = e^{-i\Delta t - \kappa/2t}. \quad (8)$$

The power spectral density for this term then takes the form

$$S_{xx}^g(\omega) = \frac{\kappa}{(\omega - \Delta)^2 + (\frac{\kappa}{2})^2}. \quad (9)$$

Similarly, for the correlation function with $A = B = n$, we have similar simplifications except for a term that scales with the mean number of photons $\bar{n} = \beta^* \beta$. The correlation function can be written as

$$C_{nn}(t) = \bar{n} \langle d(t)d^\dagger(0) \rangle = \bar{n} e^{-i\Delta t - \kappa/2t}. \quad (10)$$

The power spectral density for this second term takes the form

$$S_{nn}^g(\omega) = \frac{\bar{n}\kappa}{(\omega - \Delta)^2 + (\frac{\kappa}{2})^2}. \quad (11)$$

Finally, the cross coupling terms are computed, where we consider both $A = n, B = x$ as well as $A = x, B = n$. We find

$$C_{nx}(t) = \beta^* \langle d(t)d^\dagger(0) \rangle, \quad (12)$$

$$C_{xn}(t) = \beta \langle d(t)d^\dagger(0) \rangle. \quad (13)$$

Combining both gives

$$C_{nx}(t) + C_{xn}(t) = 2\text{Re}(\beta) e^{-i\Delta t - \kappa/2t}, \quad (14)$$

and the power spectral density becomes

$$S^{gx}(\omega) = \frac{2\text{Re}(\beta)\kappa}{(\omega - \Delta)^2 + (\frac{\kappa}{2})^2}. \quad (15)$$

Note that this term scales with $\sqrt{\bar{n}}$.

As a final step, we wish to express these three power spectral densities in terms of the drive ϵ_d . Using $\beta = \frac{\epsilon_d}{\Delta + i\frac{\kappa}{2}}$ we find

$$2\text{Re}(\beta) = \frac{2\epsilon_d \Delta}{\Delta^2 + (\frac{\kappa}{2})^2}. \quad (16)$$

Note, this only holds if ϵ_d and g share the same phase. Notice that we now have a linear dependence on detuning in the numerator and this term will change sign with Δ . Similarly, we can express \bar{n} in terms of ϵ_d as well:

$$\bar{n} = \frac{\epsilon_d^2}{\Delta^2 + \left(\frac{\kappa}{2}\right)^2}. \quad (17)$$

These three terms for the power spectral densities lead directly to Eq. (4) in the main text.

Data availability

Data for figures that support the manuscript are available at <https://doi.org/10.7910/DVN/JXLVY9>. All other data that support the findings of this paper are available from the corresponding authors upon request.

References

- Loss, D. & DiVincenzo, D. P. Quantum computation with quantum dots. *Phys. Rev. A* **57**, 120–126 (1998).
- Koppens, F. H. L. et al. Driven coherent oscillations of a single electron spin in a quantum dot. *Nature* **442**, 766–771 (2006).
- Pioro-Ladrière, M. et al. Electrically driven single-electron spin resonance in a slanting Zeeman field. *Nat. Phys.* **4**, 776–779 (2008).
- Kim, D. et al. Quantum control and process tomography of a semiconductor quantum dot hybrid qubit. *Nature* **511**, 70–74 (2014).
- Eng, K. et al. Isotopically enhanced triple-quantum-dot qubit. *Sci. Adv.* **1**, e1500214 (2015).
- Yang, C. H. et al. Silicon qubit fidelities approaching incoherent noise limits via pulse engineering. *Nat. Electron.* **2**, 151–158 (2019).
- Dohun, K. et al. Quantum control and process tomography of a semiconductor quantum dot hybrid qubit. *Nature* **511**, 70–74 (2014).
- Medford, J. et al. Self-consistent measurement and state tomography of an exchange-only spin qubit. *Nat. Nanotechnol.* **8**, 654–659 (2014).
- Wu, X. et al. Two-axis control of a singlet-triplet qubit with an integrated micromagnet. *Proc. Natl Acad. Sci. USA* **111**, 11938–11942 (2014).
- Cerfontaine, P. et al. Closed-loop control of a gas-based singlet-triplet spin qubit with 99.5% gate fidelity and low leakage. *Nat. Commun.* **11**, 4144 (2020).
- Nichol, J. M. et al. High-fidelity entangling gate for double-quantum-dot spin qubits. *npj Quantum Inform.* **3**, 3 (2017).
- Fujita, T., Baart, T. A., Reichl, C., Wegscheider, W. & Vandersypen, L. M. K. Coherent shuttle of electron-spin states. *npj Quantum Inform.* **3**, 22 (2017).
- Mills, A. R. et al. Shuttling a single charge across a one-dimensional array of silicon quantum dots. *Nat. Commun.* **10**, 1063 (2019).
- Yoneda, J. et al. Coherent spin qubit transport in silicon. *Nat. Commun.* **12**, 4114 (2021).
- Qiao, H. et al. Long-distance superexchange between semiconductor quantum-dot electron spins. *Phys. Rev. Lett.* **126**, 017701 (2021).
- Samkharadze, N. et al. Strong spin-photon coupling in silicon. *Science* **359**, 1123–1127 (2018).
- Mi, X., Cady, J. V., Zajac, D. M., Deelman, P. W. & Petta, J. R. Strong coupling of a single electron in silicon to a microwave photon. *Science* **355**, 156–158 (2017).
- Mi, X. et al. Circuit quantum electrodynamics architecture for gate-defined quantum dots in silicon. *Appl. Phys. Lett.* **110**, 043502 (2017).
- Mi, X. et al. A coherent spin-photon interface in silicon. *Nature* **555**, 599–603 (2018).
- Landig, A. J. et al. Coherent spin-photon coupling using a resonant exchange qubit. *Nature* **560**, 179–184 (2018).
- Landig, A. J. et al. Virtual-photon-mediated spin-qubit-transmon coupling. *Nat. Commun.* **10**, 5037 (2019).
- Borjans, F. et al. Split-gate cavity coupler for silicon circuit quantum electrodynamics. *Appl. Phys. Lett.* **116**, 234001 (2020).
- Borjans, F., Croot, X. G., Mi, X., Gullans, M. J. & Petta, J. R. Resonant microwave-mediated interactions between distant electron spins. *Nature* **577**, 195–198 (2020).
- Harvey-Collard, P. et al. Circuit quantum electrodynamics with two remote electron spins Preprint at <https://arxiv.org/abs/2108.01206> (2021).
- Wallraff, A. et al. Strong coupling of a single photon to a superconducting qubit using circuit quantum electrodynamics. *Nature* **431**, 162–167 (2004).
- Blais, A., Huang, R.-S., Wallraff, A., Girvin, S. M. & Schoelkopf, R. J. Cavity quantum electrodynamics for superconducting electrical circuits: An architecture for quantum computation. *Phys. Rev. A* **69**, 062320 (2004).
- Kerman, A. J. Quantum information processing using quasiclassical electromagnetic interactions between qubits and electrical resonators. *N. J. Phys.* **15**, 123011 (2013).
- Schuetz, M. J. A., Giedke, G., Vandersypen, L. M. K. & Cirac, J. I. High-fidelity hot gates for generic spin-resonator systems. *Phys. Rev. A* **95**, 052335 (2017).
- Billangeon, P.-M., Tsai, J. S. & Nakamura, Y. Circuit-qed-based scalable architectures for quantum information processing with superconducting qubits. *Phys. Rev. B* **91**, 094517 (2015).
- Didier, N., Bourassa, J. & Blais, A. Fast quantum nondemolition readout by parametric modulation of longitudinal qubit-oscillator interaction. *Phys. Rev. Lett.* **115**, 203601 (2015).
- Royer, B., Grimsmo, A. L., Didier, N. & Blais, A. Fast and high-fidelity entangling gate through parametrically modulated longitudinal coupling. *Quantum* **1**, 11 (2017).
- Ruskov, R. & Tahan, C. Modulated longitudinal gates on encoded spin qubits via curvature couplings to a superconducting cavity. *Phys. Rev. B* **103**, 035301 (2021).
- Harvey, S. P. et al. Coupling two spin qubits with a high-impedance resonator. *Phys. Rev. B* **97**, 235409 (2018).
- Mølmer, K. & Sørensen, A. Multiparticle entanglement of hot trapped ions. *Phys. Rev. Lett.* **82**, 1835–1838 (1999).
- Kirchmair, G. et al. Deterministic entanglement of ions in thermal states of motion. *N. J. Phys.* **11**, 023002 (2009).
- Häffner, H., Roos, C. & Blatt, R. Quantum computing with trapped ions. *Phys. Rep.* **469**, 155–203 (2008).
- Tinkham, M. *Introduction to Superconductivity* (Dover Books on Physics, 2004).
- Taylor, J. M. et al. High-sensitivity diamond magnetometer with nanoscale resolution. *Nat. Phys.* **4**, 810–816 (2008).
- Medford, J. et al. Scaling of dynamical decoupling for spin qubits. *Phys. Rev. Lett.* **108**, 086802 (2012).
- Dial, O. E. et al. Charge noise spectroscopy using coherent exchange oscillations in a singlet-triplet qubit. *Phys. Rev. Lett.* **110**, 146804 (2013).
- Clerk, A. A., Devoret, M. H., Girvin, S. M., Marquardt, F. & Schoelkopf, R. J. Introduction to quantum noise, measurement, and amplification. *Rev. Mod. Phys.* **82**, 1155–1208 (2010).
- Gambetta, J. et al. Qubit-photon interactions in a cavity: Measurement-induced dephasing and number splitting. *Phys. Rev. A* **74**, 042318 (2006).
- Ithier, G. et al. Decoherence in a superconducting quantum bit circuit. *Phys. Rev. B* **72**, 134519 (2005).
- Frey, T. et al. Dipole coupling of a double quantum dot to a microwave resonator. *Phys. Rev. Lett.* **108**, 046807 (2012).
- Harvey-Collard, P. et al. On-chip microwave filters for high-impedance resonators with gate-defined quantum dots. *Phys. Rev. Appl.* **14**, 034025 (2020).

46. Maleeva, N. et al. Circuit quantum electrodynamics of granular aluminum resonators. *Nat. Commun.* **9**, 3889 (2018).
47. Kamenov, P. et al. Granular aluminum meandered superinductors for quantum circuits. *Phys. Rev. Appl.* **13**, 054051 (2020).

Acknowledgements

We acknowledge useful discussions with and feedback from Y. Liu, L. Orona, A. Pierce, and N. Poniowski. This work is supported by the Quantum Science Center (QSC), a National Quantum Information Science Research Center of the U.S. Department of Energy (DOE), the Gordon and Betty Moore Foundation through Grant GBMF 9468, the National Science Foundation under Grant No. DMR-1708688, and the STC Center for Integrated Quantum Materials, NSF Grant No. DMR-1231319. S.D.B acknowledges support from the Australian Research Council (ARC) project number CE170100009.

Author contributions

C.B. and S.H. performed low-temperature measurements and fabricated the sample. S.F., G.G., and M.M. grew the wafer. C.B., S.B., and U.V. performed the data analysis and modeling. C.B., S.H., U.V. and A.Y. designed the experiment. All authors discussed the results and commented on the manuscript.

Competing interests

The authors declare no complete interests.

Additional information

Correspondence and requests for materials should be addressed to C. G. L. Böttcher.

Peer review information *Nature Communications* thanks Jian-Qiang You, and the other, anonymous, reviewer(s) for their contribution to the peer review of this work.

Reprints and permission information is available at <http://www.nature.com/reprints>

Publisher's note Springer Nature remains neutral with regard to jurisdictional claims in published maps and institutional affiliations.

Open Access This article is licensed under a Creative Commons Attribution 4.0 International License, which permits use, sharing, adaptation, distribution and reproduction in any medium or format, as long as you give appropriate credit to the original author(s) and the source, provide a link to the Creative Commons license, and indicate if changes were made. The images or other third party material in this article are included in the article's Creative Commons license, unless indicated otherwise in a credit line to the material. If material is not included in the article's Creative Commons license and your intended use is not permitted by statutory regulation or exceeds the permitted use, you will need to obtain permission directly from the copyright holder. To view a copy of this license, visit <http://creativecommons.org/licenses/by/4.0/>.

© The Author(s) 2022